

Presence of a carboxy-terminal pseudorepeat and disease-like pseudohyperphosphorylation critically influence tau's interaction with microtubules in axon-like processes

Benedikt Niewidok[†], Maxim Igaev[†], Frederik Sündermann, Dennis Janning, Lidia Bakota, and Roland Brandt^{*}

Department of Neurobiology, University of Osnabrück, 49076 Osnabrück, Germany

ABSTRACT A current challenge of cell biology is to investigate molecular interactions in sub-cellular compartments of living cells to overcome the artificial character of *in vitro* studies. To dissect the interaction of the neuronal microtubule (MT)-associated protein tau with MTs in axon-like processes, we used a refined fluorescence decay after photoactivation approach and single-molecule tracking. We found that isoform variation had only a minor influence on the tau–MT interaction, whereas the presence of a C-terminal pseudorepeat region (PRR) greatly increased MT binding by a greater-than-sixfold reduction of the dissociation rate. Bioinformatic analysis revealed that the PRR contained a highly conserved motif of 18 amino acids. Disease-associated tau mutations in the PRR (K369I, G389R) did not influence apparent MT binding but increased its dynamicity. Simulation of disease-like tau hyperphosphorylation dramatically diminished the tau–MT interaction by a greater-than-fivefold decrease of the association rate with no major change in the dissociation rate. Apparent binding of tau to MTs was similar in axons and dendrites but more sensitive to increased phosphorylation in axons. Our data indicate that under the conditions of high MT density that prevail in the axon, tau's MT binding and localization are crucially affected by the presence of the PRR and tau hyperphosphorylation.

Monitoring Editor

Erika Holzbaur
University of Pennsylvania

Received: Jun 13, 2016

Revised: Aug 3, 2016

Accepted: Aug 24, 2016

INTRODUCTION

The tau proteins are vertebrate neuronal microtubule (MT)-associated proteins (MAPs) generated by alternative splicing from a single gene (Spillantini and Goedert, 2013; Bakota and Brandt, 2016).

This article was published online ahead of print in MBoC in Press (<http://www.molbiolcell.org/cgi/doi/10.1091/mbc.E16-06-0402>) on August 31, 2016.

[†]These authors contributed equally.

^{*}Address correspondence to: Roland Brandt (brandt@biologie.uni-osnabrueck.de).

Abbreviations used: AD, Alzheimer's disease; CMV, cytomegalovirus; FDAP, fluorescence decay after photoactivation; HMM, hidden Markov model; MAP, microtubule-associated protein; MBD, microtubule-binding domain; MT, microtubule; NFT, neurofibrillary tangle; OA, okadaic acid; PAGFP, photoactivatable green fluorescent protein; PHP-tau, pseudohyperphosphorylated tau; PRR, pseudorepeat region; RR, repeat region; SM, similarity motif; SMT, single-molecule tracking.

© 2016 Niewidok, Igaev, et al. This article is distributed by The American Society for Cell Biology under license from the author(s). Two months after publication it is available to the public under an Attribution–Noncommercial–Share Alike 3.0 Unported Creative Commons License (<http://creativecommons.org/licenses/by-nc-sa/3.0>).

"ASCB®," "The American Society for Cell Biology®," and "Molecular Biology of the Cell®" are registered trademarks of The American Society for Cell Biology.

During neuronal development, tau becomes enriched in the axon, where it remains concentrated in the healthy brain. Neuronal development is also accompanied by a shift in the isoform pattern toward the expression of longer tau isoforms. In Alzheimer's disease (AD) and other tauopathies, tau redistributes from the axon to the somatodendritic compartment, where it aggregates into neurofibrillary tangles (NFTs) in a hyperphosphorylated state. Changes in tau localization and a gain of toxic function are considered to have a central role in the disease process (Rapoport et al., 2002; Roberson et al., 2007). In addition, dysfunction related to posttranslational modifications leading to MT depolymerization and impaired axonal transport may play a role (Bodea et al., 2016). Finally, transsynaptic and exosynaptic tau propagation may contribute to the disease process (Lewis and Dickson, 2016).

MTs are the most dominant binding partners of tau, with the majority of tau being associated with MTs in axons under physiological conditions (Samsonov et al., 2004; Konzack et al., 2007; Weissmann et al., 2009). Tau's functional organization with respect to its interaction with MTs has been thoroughly analyzed *in vitro*, in

silico, and in nonneuronal cell models but not in the axonal compartment. Bioinformatic and biochemical studies show that the MT-binding domain (MBD) of tau consists of three or four repeat regions (RRs), which bind to MTs via small groups of evolutionarily conserved residues (Lee *et al.*, 1989; Butner and Kirschner, 1991; Goode and Feinstein, 1994; Kadavath *et al.*, 2015a; Sundermann *et al.*, 2016). In addition, regions flanking the MBD could be important because they increase tau's assembly-promoting activity and modulate its binding to MTs in vitro and in nonneuronal cells (Brandt and Lee, 1993; Gustke *et al.*, 1994; Leger *et al.*, 1994; Preuss *et al.*, 1997). However, the extent to which these data can be extrapolated to the axonal environment in living neurons is unknown.

Tau is subject to many posttranslational modifications in health and disease, which are likely to affect its localization and function (Hasegawa *et al.*, 1992; Watanabe *et al.*, 1993; Morishima-Kawashima *et al.*, 1995; Morris *et al.*, 2015). Phosphorylation is the best-studied tau modification, and experimental evidence indicates that tau gains toxic properties in response to increased phosphorylation at disease-relevant sites (Rapoport and Ferreira, 2000; Fath *et al.*, 2002; Shahani *et al.*, 2006). Many of the physiological and pathological phosphorylation sites are located in regions that flank the MBD and might modulate tau's interaction with MTs and other cellular components (Maas *et al.*, 2000; Eidenmuller *et al.*, 2001; Ding *et al.*, 2006; Combs *et al.*, 2011; Kiris *et al.*, 2011; Xia *et al.*, 2015). Another disease-relevant posttranslational modification could be proteolytic cleavage of tau, which produces truncated tau fragments. Tau truncation appears to be an early event in AD (Reifert *et al.*, 2011; Flores-Rodriguez *et al.*, 2015) and may produce neurotoxic fragments (Park and Ferreira, 2005; Lang *et al.*, 2014), generate products that show increased release from neurons (Kanmert *et al.*, 2015), or produce fragments with a modified MT interaction (Derisbourg *et al.*, 2015). Still, the consequences of post-translational modifications of tau for its behavior in the axonal compartment remain enigmatic.

The MTs in neuronal processes have a characteristic organization, in that they form a closely packed parallel array and show a uniform plus-end-out orientation in the axon, which specialize them for efficient transport (Heidemann *et al.*, 1981; Hirokawa, 1982; Baas *et al.*, 1988). The neurites of neuronally developed PC12 cells represent a good model because the processes exhibit axon-like MT orientation (Okabe and Hirokawa, 1988). We previously showed that the organization of axonal MTs influences the way tau interacts with them and that the behavior of tau in cellular processes is noticeably different from that in vitro (Igaev *et al.*, 2014). In particular, tau interacts with MTs via a kiss-and-hop mechanism, that is, it rapidly hops between MTs, residing only transiently on each of them (Janning *et al.*, 2014). Nevertheless, it still needs to be elucidated how the interaction of tau with MTs in the axon is modulated and whether it is affected under conditions that prevail during disease such as increased phosphorylation or truncation of tau.

Among live-cell fluorescence microscopy techniques, fluorescence recovery after photobleaching (FRAP) and fluorescence decay after photoactivation (FDAP) have been applied to study tau mobility and the tau–MT interaction in living cells (Konzack *et al.*, 2007; Weissmann *et al.*, 2009; Gauthier-Kemper *et al.*, 2011; Igaev *et al.*, 2014). Tau is tagged by a variant of green fluorescent protein (GFP)—for example, enhanced GFP for FRAP and photoactivatable GFP (PAGFP) for FDAP. A defined region within the cell is irreversibly bleached or photoactivated by a focused laser flash, and the fluorescence intensity distribution as a function of time is monitored in the region of interest. The recovery/decay transient is fitted by a mathematical model to yield mobility and binding properties of the

target molecule. An advantage of fluorescence photoactivation compared with alternative methods lies in the fact that only photoactivated molecules are visible in the experimental setup. Thus newly synthesized molecules will not be fluorescent, which simplifies analysis of the results of live-cell studies (Patterson and Lippincott-Schwartz, 2002). Furthermore, photoactivation occurs more rapidly and requires lower intensity of irradiation, thereby reducing the risk of phototoxicity compared with classical photobleaching approaches (Patterson and Lippincott-Schwartz, 2002).

We used FDAP to study the functional mapping of tau's domain organization in axon-like processes. Our study reveals considerable differences to previous in vitro data. On one hand, tau isoform variation has only a minor influence on MT binding. On the other hand, MT binding is robustly enhanced by the presence of a conserved C-terminal pseudorepeat region (PRR) in tau's C-terminus in an isoform-independent manner. Disease-associated mutations in the PRR increase the dynamicity of the tau–MT interaction, whereas pseudohyperphosphorylation of tau strongly reduces MT binding. We believe that our results contribute to an understanding of the pathological processes that lead to a redistribution of tau from the axon to the somatodendritic compartment, which is one of the early events in tauopathies.

RESULTS

The presence of tau's PRR greatly enhances MT binding in axon-like processes

Human CNS tau isoforms contain an MBD in the C-terminal half of the protein that consists of three or four repeat regions (RR1–RR4; Figure 1A, left). In addition, the C-terminus contains an extra segment, which appears to be a truncated fourth repeat (pseudorepeat region [PRR]; Chapin and Bulinski, 1992). To dissect the interaction of tau with MTs in the process of living neuronal cells, we prepared a panel of C-terminal tau deletion constructs containing different numbers of RRs and the PRR. All constructs were fused to PAGFP at its amino terminus to minimize potential interference with the MT interaction. We had previously shown that such a fusion does not interfere with tau's interaction with axonal membrane components, which is mediated by the amino-terminal projection domain and contributes to tau's localization in the neuronal process (Weissmann *et al.*, 2009; Gauthier-Kemper *et al.*, 2011). The constructs were present as single polypeptides in transfected PC12 cells, indicating their integrity. They separated at a 40–50% higher molecular weight than calculated from their sequence (Figure 1A, right), which is in agreement with earlier studies (Maas *et al.*, 2000; Weissmann *et al.*, 2009).

After neuronal differentiation of transfected PC12 cells, PAGFP was activated within a segment in the middle of the process by a laser flash at 405-nm wavelength (Figure 1B), and FDAP was recorded in the activated region as a function of time (Figure 1C, left). The FDAP decay can be used as a measure of protein dynamics in the corresponding cellular compartment. Deletion of tau's extreme C-terminus (tau Δ 401) yielded a construct that exhibited a slower decay than wild-type (wt) tau (tau441wt), indicating enhanced binding ability of tau Δ 401 (red vs. black curve in Figure 1C, left). In contrast, further deletion resulting in the removal of the PRR (tau Δ 369) led to a much faster decay than with tau Δ 401 and tau441wt (dark blue vs. red and black curves in Figure 1C, left). Calculation of the effective diffusion constant (Weissmann *et al.*, 2009) yielded $D_{\text{eff}} = 0.22 \pm 0.01 \mu\text{m}^2/\text{s}$ (mean \pm SEM, $n = 26$) for full-length tau (tau441wt). Comparing the values for the different constructs confirmed the influence of the PRR and indicated that its deletion increased D_{eff} by a factor of ~ 17 ($D_{\text{eff}} = 1.41 \pm 0.20$ and $0.06 \pm 0.04 \mu\text{m}^2/\text{s}$ for tau Δ 369 and tau Δ 401, respectively; Figure 1C, right). Further deletions moderately increased D_{eff} .

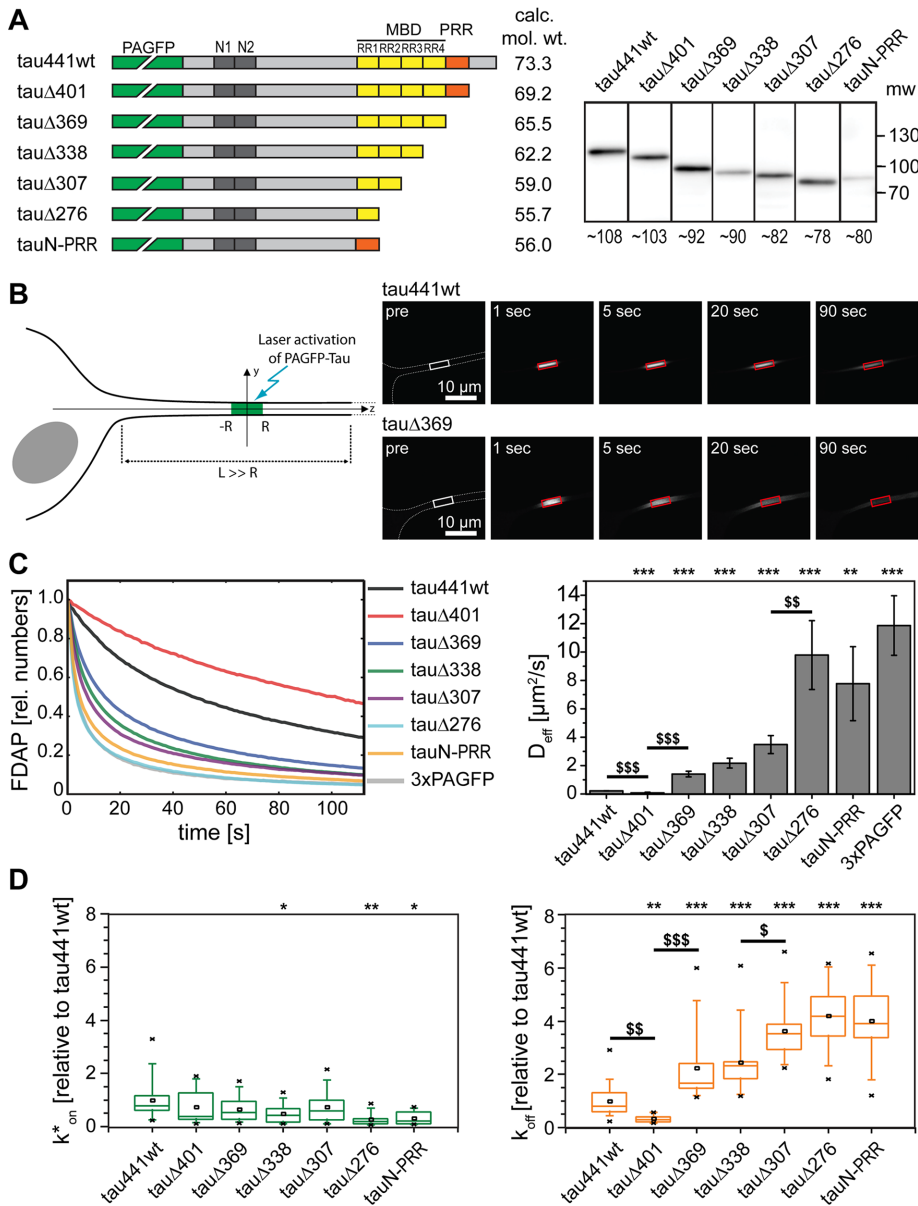


FIGURE 1: Tau's PRR greatly enhances MT binding in processes of living neuronal cells. (A) Schematic representation of the tau deletion constructs with N-terminal PAGFP fusion. The MT-binding repeat regions (RR1–RR4) are indicated by the yellow boxes and the PRR by the orange box. Adult-specific exons in the N-terminus are shown in dark gray (N1, N2). Right, immunoblots of cellular lysates after transfection with the respective tau constructs. Detection used anti-GFP antibody. Molecular weight standards are indicated on the far right, and respective molecular weights as determined from the electrophoretic separation are indicated beneath. (B) Schematic representation of the photoactivation approach (left) and representative time-lapse recordings of fluorescence distribution after expression of PAGFP-tau441wt and -tauΔ369 (right). Photoactivation was performed in a neuronally differentiated PC12 cell. A segment of 2R in length in the middle of a cellular process of length L ($L \gg R$) was photoactivated, and the fluorescence distribution was monitored over time. Dashed white line, outline of the cell; white box, region of activation; red box, region of fluorescence recording. (C) FDAP plots (left) and a diagram of the effective diffusion constants (right) for the different constructs. Values are mean \pm SEM (error bars). (D) Bar plots showing k^*_{on} and k^*_{off} values of the respective constructs. The numbers are relative to tau441wt. The box represents 50% of the population, whiskers range from 5 to 95%, crosses correspond to the minimal and maximal values, the horizontal line shows the median, and the black square shows the mean value. Statistically significant differences relative to full-length tau (tau441wt) are indicated on top (asterisks) and between neighboring columns by dollar signs. Reference values for full-length tau (tau441wt) were determined from three independent sets of cells, with 9–13 cells/set. For other constructs, 6–23 cells were evaluated. * $p < 0.05$, ** $p < 0.01$; *** $p < 0.001$.

A second major increase of D_{eff} was observed for a construct containing only one RR (tauΔ276; Figure 1C, right). This might imply a special role for RR2, which is present only in the adult-specific four-repeat tau isoforms, or might be due to a requirement of at least two repeat regions for efficient binding. A construct similar to tauΔ276 in which RR1 was replaced by the PRR (tauN-PRR) did not exhibit stronger binding than tauΔ276, indicating that the PRR requires the presence of other repeats to exert its function as an amplifier of the MT interaction.

A rigorous treatment of FDAP data requires that the general reaction-diffusion equations describing the underlying protein dynamics be solved (Sprague et al., 2004). The method introduced by Weissmann et al. (2009) relies on an approximation to the full reaction-diffusion system and does not allow an assessment of both association (k_{on}) and dissociation (k_{off}) constants, which directly reflect the on-off dynamics of tau on MTs. Furthermore, using this kind of FDAP data treatment makes it impossible to cross-correlate the results with more precise fluorescence methods for studying binding kinetics, such as single-molecule tracking (SMT) microscopy. We used a previously developed refined reaction-diffusion model of the tau–MT interaction (Igaev et al., 2014) to directly estimate the pseudo-first-order association rate ($k^*_{on} = k_{on}[MT]_{eq}$, where $[MT]_{eq}$ is the equilibrium concentration of tau-binding sites on MTs) and the dissociation rate (k^*_{off} ; also measurable by SMT) for all of the introduced constructs (Figure 1D). Of note, the presence of the PRR did not influence k^*_{on} but led to a remarkable change in k^*_{off} , as indicated by a greater-than-sixfold increase upon deletion (2.20 ± 0.38 and 0.33 ± 0.05 s $^{-1}$ for tauΔ369 and tauΔ401, respectively); k^*_{off} is expressed relative to the value for tau441wt, which was set to 1.0). This indicates that the PRR amplifies tau's binding to MTs by keeping it longer in the MT-bound state while having no influence on the association process of tau to MTs.

Isoform variation only moderately affects tau's interaction with MTs in neuronal processes

The data indicate that the presence of three or four RRs in the MBD has only a moderate effect on the tau–MT interaction in neuronal processes. This is exemplified by our observation that a deletion construct containing four RRs (tauΔ369) exhibits only a slightly lower D_{eff} than the construct with three RRs (tauΔ338), with no major change in either k^*_{on} or k^*_{off} (Figure 1D).

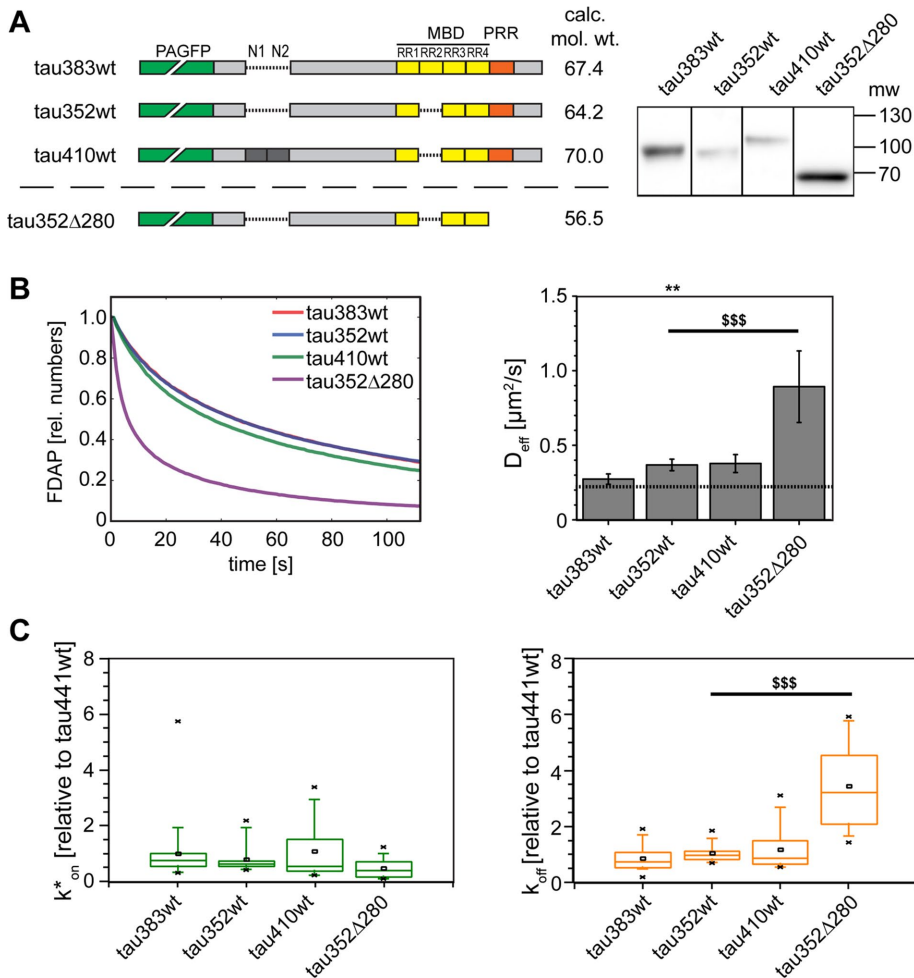


FIGURE 2: Isoform variation only moderately affects the tau–MT interaction in axon-like processes. (A) Schematic representation of the different CNS tau isoforms and a C-terminal deletion construct of the shortest tau isoform (left). The isoforms differ by the presence or absence of RR2 and adult-specific exons in the N-terminus (N1, N2). Right, immunoblot analysis of cellular lysates after transfection with the respective tau constructs. Detection used anti-GFP antibody. Molecular weight standards are indicated on the far right. (B) FDAP plots (left) and a diagram of the effective diffusion constants (right) for the different constructs. Note that the decay curves of tau383wt and tau352wt run together. Values are shown as mean \pm SEM (error bars). Statistically significant differences of the isoforms relative to full-length tau (tau441wt; indicated by dotted line) are indicated by asterisks and between columns by dollar signs. (C) Bar plots showing k^*_{on} and k^*_{off} values of the respective constructs. The numbers are expressed relative to tau441wt. The reference value for full-length tau (tau441wt) and the meaning of the box plot are explained in the legend to Figure 1. For the isoforms and the deletion construct, 10–45 cells were evaluated per set. ** $p < 0.01$; \$\$\$ $p < 0.05$.

To address directly the question how isoform variation affects the interaction, we tested constructs containing or lacking the alternatively spliced exons in the N-terminus (N1, N2) and the MBD (RR2). For further comparison, we also prepared a construct lacking all alternatively spliced exons and the C-terminus including the PRR (Figure 2A, left). All constructs were expressed in PC12 cells at the expected size with no obvious degradation (Figure 2A, right). The FDAP curves for the different isoforms were very similar, and only the deletion constructs lacking the PRR (tau352Δ280) exhibited clearly increased decay (Figure 2B, left, purple curve), similarly to the respective four-repeat isoforms (tauΔ369 vs. tau441wt; Figure 1C). Determination of D_{eff} revealed that the fetal tau isoform (tau352wt) showed a small but significant increase compared with tau441wt. Deletion of the C-terminus containing the PRR had

a much stronger influence compared with its full-length counterpart (tau352wt). The presence or absence of N1 and N2 did not influence the MT binding of tau. Calculating k^*_{on} and k^*_{off} confirmed the similar behavior of the tau isoforms, whereas deletion of the PRR led to a significant decrease in k^*_{off} of the three-repeat constructs (Figure 2C), in agreement with results for constructs containing four RRs (Figure 1D).

The PRR is highly conserved and constitutes a separate group in nearest-neighborhood cluster analysis

We showed that the PRR has a dramatic effect on MT binding compared with other RRs, as indicated by a greater-than-sixfold increase in k^*_{off} upon deletion. This raises questions about similarities between the RRs and the PRR.

A generalized hidden Markov model (HMM) of the RR sequence was constructed as described in *Materials and Methods* and used to extract RR-similar sequences from 49 mammalian full-length sequences of MAP (Figure 3A). Similarity relations were determined using a nearest-neighborhood cluster analysis of the extracted RR-similar amino acid sequences. Remarkably, the cluster analysis identified the PRR as a fifth group along with the common four RRs, with RR4 being most similar to the PRR (Figure 3B).

Our initial definition of the PRR implied that it is of similar length to other RRs. To determine the exact size of the most similar motif, the HMM-HMM comparison method proposed by Soding (2005) was used. As a target HMM, the generalized HMM (Figure 3A) was used, and the size of the PRR was determined using an iterative comparison approach (*Materials and Methods*). The similarity was highest at a length of 18 amino acids (aa; Figure 3C). This was used to create a HMM of the similarity motif (SM) from mammalian tau sequences (Figure 3D). The position of the SM in the human tau sequence is indicated below the HMM logo.

Tau belongs to a family of structural MAPs that share a conserved C-terminal domain containing the MT-binding domain. The family consists of the neuronal MAPs tau and MAP2 and the non-neuronal MAP4 (Dehmelt and Halpain, 2005; Sundermann et al., 2016). To determine phylogenetic conservation of the SM, we compared the SM's HMM from mammalian tau with those of tau from other classes (Aves, Reptilia, Actinopterygii) and generalized HMMs of MAP2 and MAP4. The results indicate that the SM is highly conserved across all classes in MAP tau (MAPT) and is also present in MAP2 and MAP4, suggesting that it serves as a general modulator of the MT interactions in all members of the MAPT/MAP2/MAP4 family. Of interest, the comparison also revealed a high similarity of the SM of tau to the RR4 of MAP2, supporting their close relation (Figure 3E).

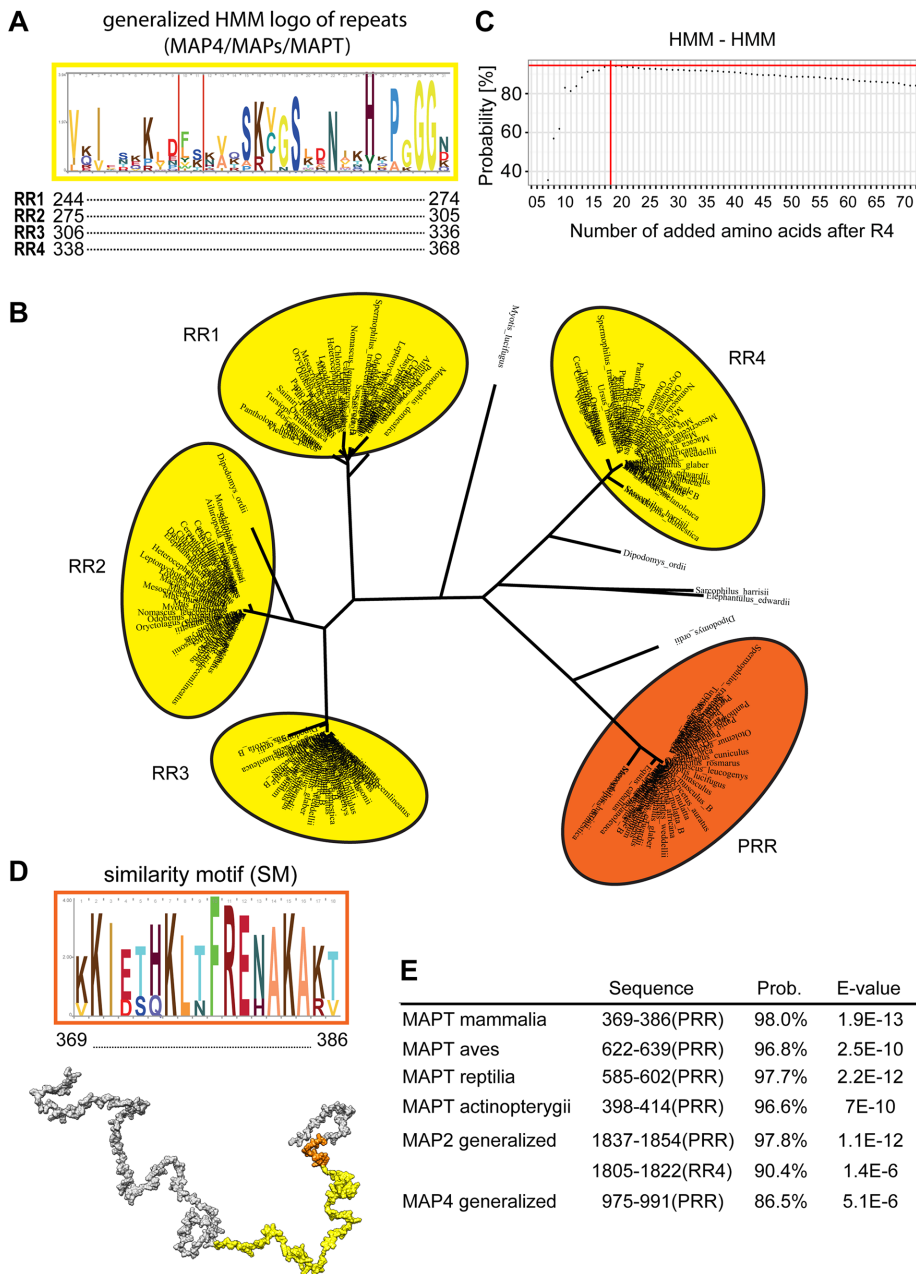


FIGURE 3: The PRR is highly conserved and constitutes a separate group in nearest-neighborhood cluster analysis. (A) HMM logo of the generalized Pfam (PF00418) seed alignment of the RRs. The position of the respective RR in human tau is shown at the bottom. (B) Unrooted tree of the RRs and the PRR of mammalian tau to visualize the relation between these regions. The colored groups refer to the sequences included in further analysis. (C) Similarity of the mammalian PRR with the generalized Pfam HMM of the repeat regions determined by HMM-HMM comparison. The probability value as a measure of HMM similarity is plotted vs. number of amino acids consecutively added after the RR4. Red lines, position in the amino acid sequence at which the maximal probability is reached. (D) HMM logo of the 18-amino acid SM as determined in C. The position of the SM in human tau is shown beneath. Bottom, representative 3D structure of tau based on the RCG model. The MBD (yellow) and SM (orange) were mapped onto the structure. The end-to-end distance (distance between amino acids 1 and 441) is ~25 nm. (E) Comparison of the SM with the MAPT HMMs of mammals, birds, reptiles, and ray-finned fish, as well as with generalized MAP2 and MAP4 HMMs.

Pseudophosphorylation at the PHF-1 site does not affect MT interaction

The data indicate that the presence of the PRR (aa 369–400) strongly enhances tau's interaction with MTs. It is therefore presumable that

displayed much higher on- and off rates than with tau441wt, indicating that, although the overall binding is not changed, the mutations induce a higher dynamicity of the tau-MT interaction in axon-like processes.

tau's MT interaction is regulated by phosphorylation in this region. Of interest, two disease-associated phosphorylation sites that are detected by the PHF-1 antibody occur in or close to the PRR. The PHF-1 antibody detects paired helical filaments of AD patients, recognizes NFTs and pretangles in various mouse models, and was used for immunization experiments aimed at decreasing tau pathology (Lewis *et al.*, 2000; Augustinack *et al.*, 2002; Boutajangout *et al.*, 2011; Mondragon-Rodriguez *et al.*, 2014). To test the hypothesis that phosphorylation at the PHF-1 epitope affects the activity of the PRR to amplify tau-MT binding, we prepared tau mutants in which phosphorylation was either mimicked or blocked at the PHF-1 site (positions S396 and S404; Otvos *et al.*, 1994).

We did not detect a significant difference between phosphomimicking (tau441_{S396E/S404E}) and phosphoblocking tau mutants (tau441_{S396A/S404A}) in FDAP experiments, which was evident from similar D_{eff} values for the respective constructs (Figure 4A, left and middle). In addition, extraction of the on- and off-rates from the decay curves indicated a very similar behavior of the two constructs (Figure 4A, right), suggesting that the amplifying effect of the PRR is robust against the phosphorylation state of the PHF-1 epitope. The results are consistent with previous *in vitro* data, for which phosphomimicking mutations in the PHF-1 site had been combined with mutations in other epitopes recognized by Alzheimer diagnostic antibodies (AT8, AT100); here only small effects on MT polymerization were observed (Jeganathan *et al.*, 2008).

Hereditary tauopathy mutations located in the PRR do not affect apparent MT binding but increase the dynamicity of the interaction

Two hereditary tauopathy mutations were previously reported in the PRR, K369I and G389R (Ghetti *et al.*, 2000; Neumann *et al.*, 2001). In cell-free assays, both mutations reduced the ability of tau to promote MT assembly. To test whether these mutations affect tau's MT interaction in axon-like processes, we prepared tau expression constructs with the respective amino acid exchanges and tested them using our FDAP approach. Both mutants exhibited very similar FDAP decays and did not show a significant difference from the wild-type construct as judged from D_{eff} (Figure 4B, left and middle). However, both constructs

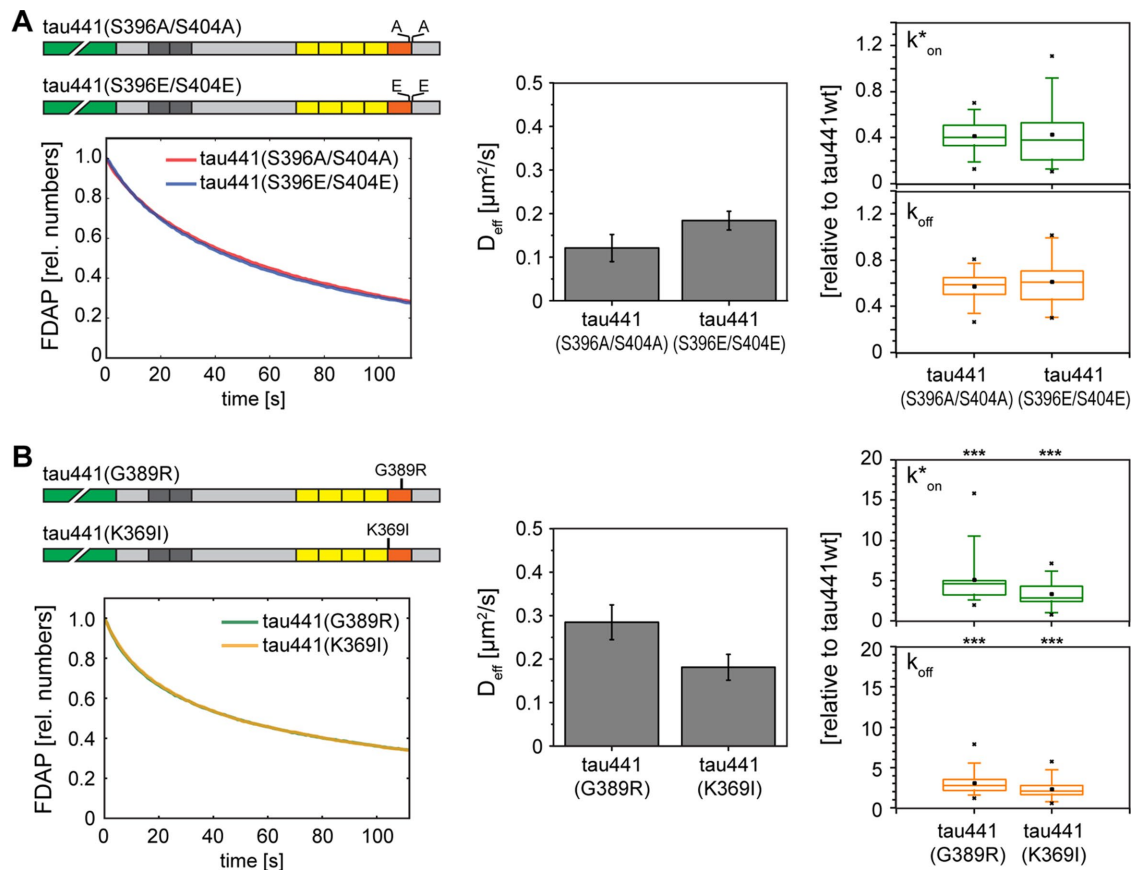


FIGURE 4: Effect of phosphomutations at the PHF-1 site and hereditary tauopathy mutations on the tau–MT interaction in neuronal processes. (A) Left, schematic representation of the tau phosphomutants (top) and FDAP plots (bottom) for the respective constructs. Middle, effective diffusion constants of the two phosphomutants. Right, bar plots with k_{on}^* and k_{off} values of the two constructs. (B) The hereditary tauopathy mutations, FDAP plots, a diagram of the effective diffusion constants, and bar plots with k_{on}^* and k_{off} values. The D_{eff} values are shown as mean \pm SEM (error bars). For the bar plots, the numbers are expressed relative to tau441wt. Statistically significant differences relative to tau441wt are indicated at the top by asterisks. The meaning of the box plot is explained in the legend to Figure 1. For the experiments, 8–23 cells (phosphomutants) and 15–30 cells (hereditary tauopathy mutations) were evaluated. *** $p < 0.001$.

Disease-like tau hyperphosphorylation in regions flanking the RRs and the PRR weaken tau–MT interaction by a strong decrease of k_{on}^*

We demonstrated that phosphorylation at the disease-relevant PHF-1 site has no major influence on the tau–MT interaction in neurites. This poses the question of the extent to which other disease-relevant phosphorylation events, in particular an AD-like tau hyperphosphorylation, affect binding of tau to MTs.

Previously we prepared tau constructs in which 10 serine/threonine residues that are phosphorylated to a high extent in PHF-tau isolated from patients with AD were substituted with glutamate to create a pseudohyperphosphorylation of these residues. We showed that such pseudohyperphosphorylated tau constructs (PHP-tau) mimic key structural and functional aspects of hyperphosphorylated tau (Eidenmuller *et al.*, 2000, 2001; Maas *et al.*, 2000). Cell culture experiments using PHP-tau provided evidence for a neurotoxic effect of soluble tau as a result of structural changes induced by cumulative, high-stoichiometric, and stable tau phosphorylation (Fath *et al.*, 2002; Shahani *et al.*, 2006; Tackenberg and Brandt, 2009; Golovyashkina *et al.*, 2015). In a transgenic *Caenorhabditis elegans* model, PHP-tau induced a developmental defect (Brandt *et al.*, 2009), and we observed altered tau phosphorylation at additional, nonmodified sites in transgenic mice (Hundelt *et al.*, 2011).

In our FDAP experiments, tau441PHP exhibited a much more rapid fluorescence decay than tau441wt, indicating a weakened interaction with MTs (Figure 5A). In fact, D_{eff} of the pseudohyperphosphorylated construct was approximately three times as high as for wild-type tau (Figure 5B). Further analysis showed that the increased D_{eff} was mostly due to a decreased k_{on}^* rate, whereas k_{off} increased only slightly without reaching significance (Figure 5C). To cross-validate our FDAP measurements and determine the residence time of tau on MTs ($1/k_{off}$), we used SMT analysis in which substoichiometrically labeled, Halo-tagged tau molecules were followed at high spatiotemporal resolution (Janning *et al.*, 2014). PHP-tau rapidly moved within some tens of milliseconds between binding sites that were several hundred nanometers apart, suggesting rapid, undirected movement of tau molecules both longitudinally and transversally (Figure 5D, left). This movement corresponded to the same kiss-and-hop interaction that we previously described for wild-type tau (Janning *et al.*, 2014). Quantification revealed a mean residence time of 27 ms for PHP-tau (Figure 5D, right), which was only slightly lower than the value for the wild-type construct (38 ms, as reported previously). Thus the SMT data support the finding that the increase of D_{eff} for tau441PHP was mainly due to a massive decrease in the k_{on}^* rate. Although it is clear that PHP-tau is different from real pathological tau, the data are consistent with the view that disease-like tau modifications alter the way in which tau interacts with MTs, thereby facilitating a loss of tau from axonal MTs.

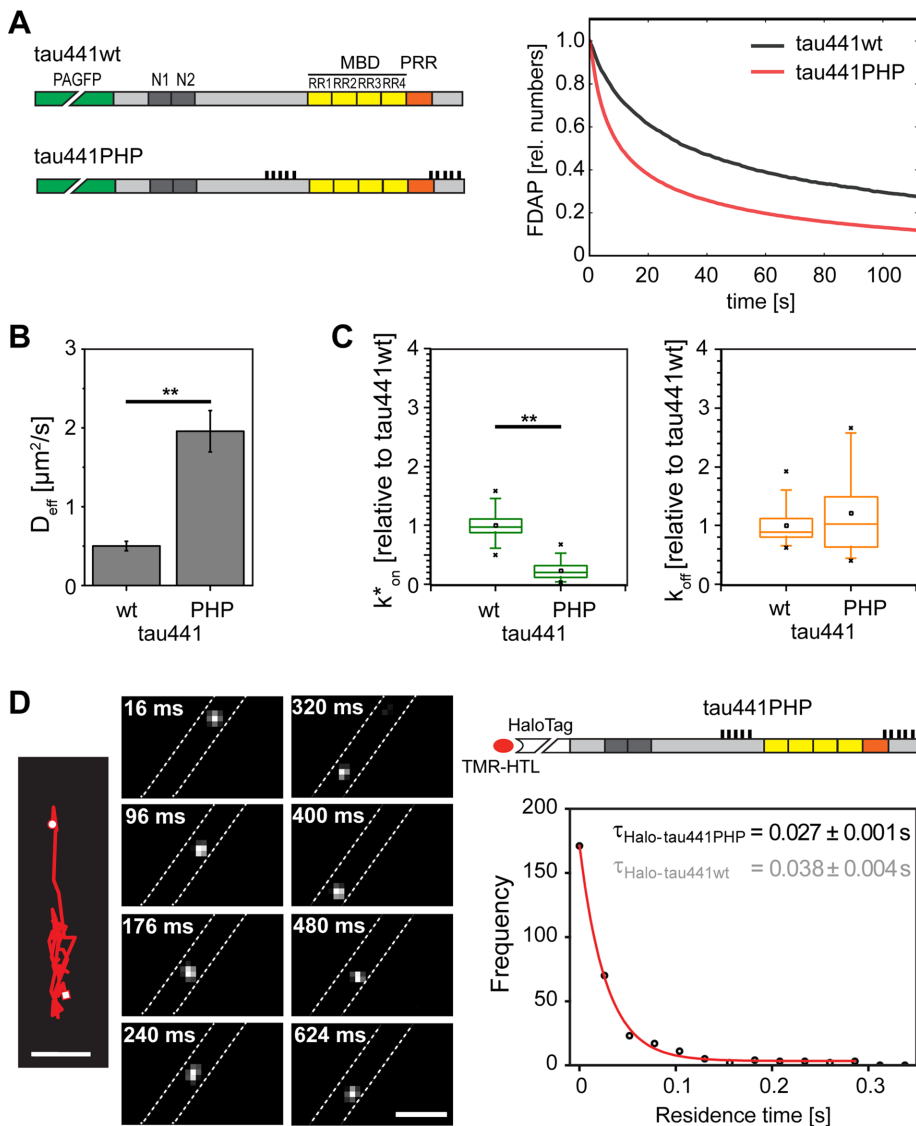


FIGURE 5: Disease-like tau hyperphosphorylation in regions flanking the RRs and the PRR weakens the tau–MT interaction by a strong decrease of the k_{on}^* -rate. (A) Schematic representation of wt and PHP tau (left) and FDAP plots (right) for the respective constructs. The 10 positions with serine/threonine-to-glutamate exchange are indicated by vertical lines. (B) Effective diffusion constants of wt and PHP tau. Values are as mean \pm SEM (error bars). (C) Bar plots showing k_{on}^* and k_{off} values of the two constructs. The numbers are expressed relative to tau441wt. (D) Schematic representation of the Halo-tagged PHP-tau fusion construct (top right) and time series of individual Halo-PHP tau molecule moving in a process of a neuronally differentiated PC12 cell (left). Dashed lines indicate the border of the process. A trajectory generated from the complete time series (2.2 s = 440 frames) is shown at the far left, indicating an undirected, fast movement both longitudinally and transversally. The starting point is indicated by a circle and the end by a square. Scale bar, 0.5 μm . Bottom right, representative histogram of residence times of tau on MTs in PC12 cells. The single-exponential fit is indicated by a red line, and the time constant (residence time) is given on top. The residence time of wt tau was determined previously (Janning *et al.*, 2014) and is indicated in gray. Mean \pm SEM is shown ($n = 3$). The meaning of the box plot is explained in the legend to Figure 1. ****** $p < 0.01$.

Tau exhibits similar apparent MT binding in axons and dendrites that is more sensitive to increased protein phosphorylation in the axon

PC12 cells develop axon-like processes but do not show differentiation into axonal and somatodendritic compartments. To determine whether tau–MT interaction is compartment specific, we used primary cortical cultures from mice. To exclude potential

interference with endogenous mouse tau, we prepared the cultures from tau-knock-out mice and expressed PAGFP-tagged human tau (tau441wt) using a lentivirus. Axons and dendrites could be clearly distinguished using morphological criteria, with axons establishing a long process with uniform diameter and rectangular ramification, whereas dendrites showed a tapered morphology with branched cell processes (Figure 6A, left, arrow vs. arrowhead). Photoactivation was performed in $\sim 6\text{-}\mu\text{m}$ -long, straight segments of the respective processes, and the fluorescence distribution was followed over 112 s (Figure 6A, right).

The FDAP decays for both axonal and dendritic tau were similar, which resulted in similar values for D_{eff} (Figure 6, B and C). The apparent association and dissociation rates as extracted in our FDAP analysis are directly proportional to the MT density (Igaev *et al.*, 2014). Taking into account published data on the distance between MTs in axons and dendrites from rat brain (20–30 vs. 60–70 μm , respectively; Chen *et al.*, 1992), we can estimate real kinetic constants of 83.5 (axon) and 460.9 s^{-1} (dendrite) for the pseudo-association rate and 3.3 (axon) and 20.8 s^{-1} (dendrite) for the dissociation rate. The values clearly differ between these compartments and may be due to the generally higher phosphorylation state of dendritic tau (Papasozomenos and Binder, 1987; Mandell and Banker, 1996; Maas *et al.*, 2000).

To determine the potential effect of increased phosphorylation, we treated the cultured neurons with the phosphatase inhibitor okadaic acid (OA) before imaging. The OA treatment increased the mobility of PAGFP-tau in both compartments, indicating a weakened MT interaction (Figure 6B). Extraction of the on- and off-rates from the FDAP curves showed that the effect of phosphorylation was much more pronounced in the axonal compartment, in which OA induced a twofold-to-threefold increase in on- and off-rates (2.39 and 2.69 s^{-1} , respectively), whereas the change was <1.5 in dendrites (1.09 and 1.45 s^{-1} , respectively; Figure 6D). Thus the data suggest that tau–MT interaction in the axon is more sensitive to increased phosphorylation than in the dendrite. Note, however, that OA is likely to

change the phosphorylation state of many proteins in addition to tau and that the effect of OA on tau depends on the basal phosphorylation of many individual sites.

DISCUSSION

The neuronal axon represents a unique cellular compartment, as it contains an array of densely packed, parallel MTs specialized

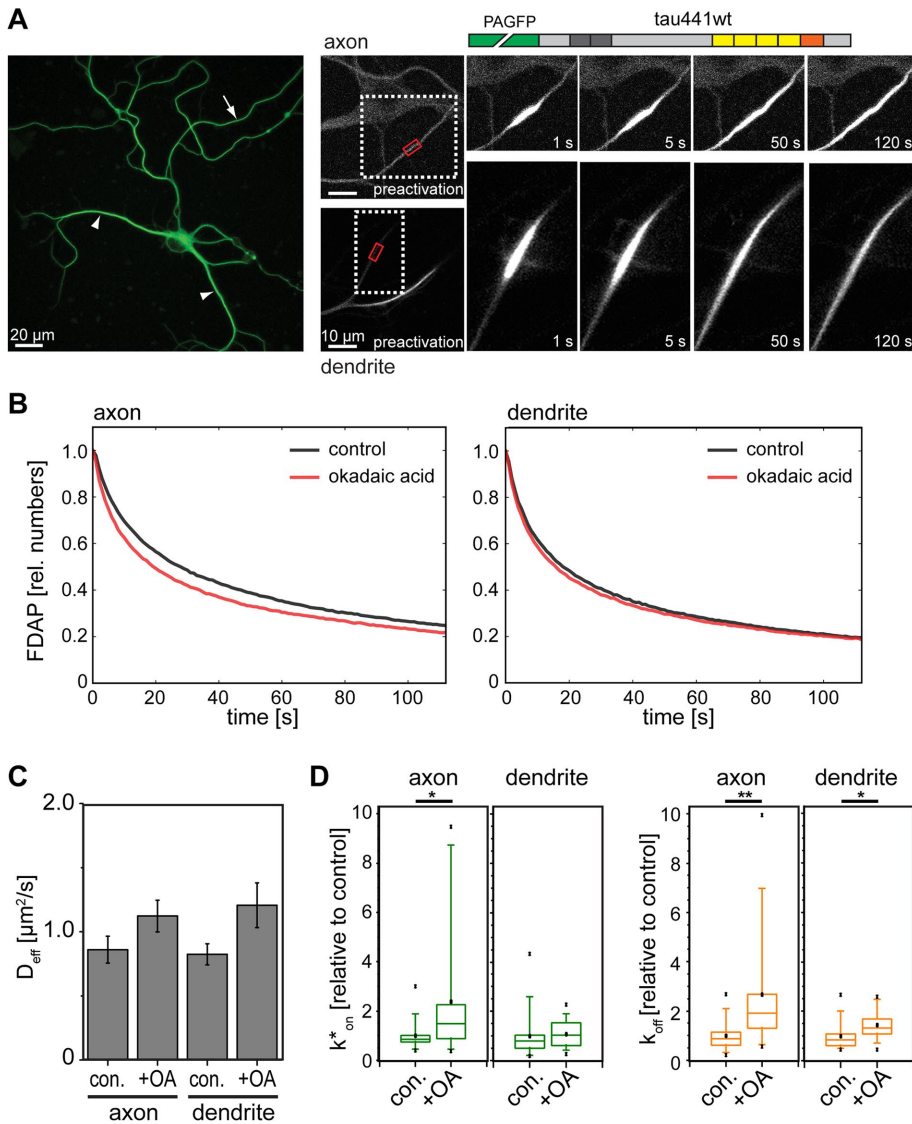


FIGURE 6: Tau exhibits similar apparent MT interaction in axons and dendrites that is sensitive to okadaic acid-induced increase in intracellular protein phosphorylation. (A) Example image of a primary cortical neuron lentivirally infected to express PAGFP-tau441wt (left). The neuron was photoactivated before imaging. The axon (arrow) and dendrites (arrowheads) are indicated. Right, representative time-lapse recording of the fluorescence distribution in the axon (top) or dendrite (bottom). (B) FDAP plots after photoactivation in the axon or dendrites of control cultures or cultures treated with okadaic acid. (C) Effective diffusion constants and (D) bar plots showing k_{on}^* and k_{off} values. The numbers in the bar plots are expressed relative to the respective control experiment (without okadaic acid). For the experiments, 39–54 processes were evaluated for each condition and compartment. The meaning of the box plot is explained in the legend to Figure 1. * $p < 0.05$, ** $p < 0.01$.

for structural stabilization and efficient transport over long distances. Under physiological conditions, the axon is the natural environment for the majority of the MT-associated protein tau. We previously addressed the paradox that tau, although mostly bound to MTs at every time point, does not interfere with MT-dependent transport. The explanation is the kiss-and-hop mechanism, according to which tau rapidly interconverts between free and MT-bound states with a dwell time of ~40 ms on a single MT (Igaev et al., 2014; Janning et al., 2014). Here we addressed how the binding of tau is regulated and how disease-like modifications affect the tau–MT interaction in axon-like processes.

Our refined FDAP approach allows us to determine several functional parameters of the tau–MT interaction in living cells, providing a more precise understanding of tau’s behavior in neuronal compartments. Our major findings are as follows: 1) tau isoform variation has only a minor effect on its MT interaction in axon-like processes; 2) the presence of a conserved PRR at tau’s extreme C-terminus greatly enhances MT binding by decreasing the dissociation rate; 3) disease-associated tau mutations in the PRR do not influence apparent MT binding but increase the dynamicity of the tau–MT interaction; 4) simulation of a disease-like tau hyperphosphorylation dramatically diminishes the association rate of tau to MTs but does not change the kiss-and-hop nature of this interaction; and 5) the apparent tau–MT binding is similar in axons and dendrites but is more sensitive to increased phosphorylation in the axon.

In the CNS, tau is present in six isoforms, which differ by the presence or absence of three alternatively spliced exons. With respect to the MT association, exon 10, which codes for an additional repeat region (RR2), has been in the focus of intense research. Interest has also been provoked by the finding that some tauopathies are associated with a misbalance in isoform expression toward four-repeat isoforms by inclusion of exon 10 (Spillantini and Goedert, 2013). Previously, using a fixation protocol after microinjection of recombinant tau constructs, K_D values of 1.1 and 2.5 μM were estimated for 441wt and 352wt tau, respectively, in the cytosol of cultured cells (Preuss et al., 1997), suggesting some difference in binding. The difference in K_D corresponds to in vitro data, for which an approximately threefold increase in binding activity of 4R- versus 3R-tau has been reported (Butner and Kirschner, 1991; Gustke et al., 1994). Our FDAP data from axon-like processes indicate an increase of only ~1% in the amount of MT-bound tau for the 4R- compared with the 3R-isoform. Therefore, in contrast to the conditions in vitro and in the cell body, isoform variation has only a minor effect on MT binding in the presence of the densely packed MT arrays that prevail in the axon. Thus isoform variation is unlikely to affect the axonal localization of tau but might modulate other properties of the axonal MT array, such as by determining the spacing between MTs or mitochondrial localization (Bunker et al., 2004; Stoothoff et al., 2009; Chung et al., 2015).

As discussed earlier, we observed considerable differences between our results on the interaction of tau with MTs in living cells and previous in vitro binding studies. Among the reasons for disagreement could be that in vitro binding studies mostly used Taxol-stabilized MTs. It is known, however, that Taxol induces structural changes in the MT lattice (Nogales et al., 1995; Xiao et al., 2006), and we and

others previously showed that treatment of cells with Taxol results in a detachment of tau from MTs, which decreases the fraction of MT-associated tau by almost 20% (Samsonov *et al.*, 2004; Weissmann *et al.*, 2009). In fact, it was also reported that the apparent tau–MT affinity as determined *in vitro* depends on the methods and protein concentrations used and that Taxol-stabilized MTs can even promote tau filament formation (Duan and Goodson, 2012). Of interest, tau's ability to promote MT assembly under Taxol-free conditions appears to better reflect its interaction in cells, as evidenced by a similar critical concentration of tau-dependent MT assembly for the 3R and 4R isoforms (Brandt and Lee, 1993; Panda *et al.*, 2003).

In contrast to the effect of exon 10, truncation of a pseudorepeat region at tau's C-terminus strongly diminished the tau–MT interaction by a more-than-sixfold increase of the dissociation rate. We and others previously showed that regions flanking tau's MT-binding domain modulate MT-related activities of tau *in vitro* and in nonneuronal cells (Brandt and Lee, 1993; Gustke *et al.*, 1994; Preuss *et al.*, 1997; Goode *et al.*, 2000). However, the strong effect of the PRR is also surprising with respect to previous observations *in vitro* in which the C-terminal tail increased the MT association of 3R-tau but had only a negligible effect for 4R-tau (Goode *et al.*, 2000). In contrast, our data show that deletion of the C-terminal tail strongly decreases tau's MT binding for both the 3R- and the 4R-isoforms (Figures 1C and 2B), suggesting that this region amplifies tau's interaction with the axonal MT array independent of the isoform and could be important for retaining tau in the axonal compartment. Our data are consistent with results from recent *in vitro* experiments in which regions involved in tau's binding to MTs have been identified by nuclear magnetic resonance (Kadavath *et al.*, 2015a,b). Here signal broadening indicative for MT interaction was also observed for tau residues 375–398, which are located in the PRR, and cross-links of Lys-383 to tubulin were reported.

Conditions that affect the integrity of the PRR could have a critical role in triggering the redistribution of tau during tauopathies. In fact, C-terminal truncation of tau at the caspase-3 cleavage site located at Asp-421 appears to be an early event in disease (Flores-Rodriguez *et al.*, 2015) and might link amyloid β and tau pathology (Gamblin *et al.*, 2003). Furthermore, the tau fragment within the core of PHFs has been identified to be C-terminally truncated at Glu-391 (Wischnik *et al.*, 1988), a position that is located within the PRR. In addition, C-terminal cleavage might also facilitate the release of tau from neurons, since secreted tau species have been described as being C-terminally truncated (Kanmert *et al.*, 2015). Thus disease-related C-terminal truncation of tau could initiate a multitude of potentially disease-relevant events, including diminished axonal MT binding and neuronal release.

Bioinformatic analysis revealed the PRR as a fifth homology group in addition to the common four RRs and identified an 18-amino acid long motif (SM) with high similarity across different tau species. The SM was also highly homologous to the corresponding region in other members of the MAPT/MAP2/MAP4 family. It was previously assumed that the nonneuronal MAP4 is unique and contains no sequence similarity in the respective region (Chapin and Bulinski, 1992). However, we identified a similar motif in MAP4, which suggests that this modulating region is present in the nonneuronal MAP4 as well. Thus it appears that the SM developed early during evolution before the diversion of the neuronal MAPs at the dawn of the vertebrates (Dehmelt and Halpain, 2005; Sundermann *et al.*, 2016).

Simulation of a disease-like hyperphosphorylation using a model of pseudohyperphosphorylated tau did not affect the kiss-and-hop characteristics of the tau–MT interaction but caused a strong decrease of MT binding, which was attributed mainly to a decrease in

the association rate. In contrast, hereditary tau mutations at the PRR did not affect tau's overall MT binding but increased the dynamicity of the interaction with MTs in axon-like processes. In some cases, the G389R mutation was associated with an extreme early onset of dementia that developed in juvenile patients (Birmingham *et al.*, 2008; Chaunu *et al.*, 2013). This could indicate that changes in the dynamicity of tau's axonal MT interaction rather than effects on overall MT binding have a decisive role in the development of tauopathies.

We showed that, despite different intermicrotubule distances, overall apparent tau–MT binding is similar in axons and dendrites. This implies that the real kinetic constants of tau differ between these compartments, which may be due to the higher phosphorylation state of dendritic tau (Papasozomenos and Binder, 1987; Mandell and Banker, 1996; Maas *et al.*, 2000). Note, however, that spacing between MTs may become much larger during aging and neurodegenerative conditions since significant MT reduction in both density and length was observed in human pyramidal neurons during AD and aging (Cash *et al.*, 2003). In addition, MT dynamicity appears to increase with age and in pathological conditions (Penazzi *et al.*, 2016a,b). The change in MT spacing will affect the apparent association and dissociation rates of tau and could affect the influence of mutations or phosphorylation on the interaction with the axonal MT array, thereby contributing to mislocalization of tau under pathological conditions.

MATERIALS AND METHODS

Materials and antibodies

Chemicals were obtained from Sigma-Aldrich (Deisenhofen, Germany), and cell culture media, supplements, culture flasks, plates, and dishes were obtained from Sigma-Aldrich and ThermoFisher Scientific (Schwerte, Germany), unless stated otherwise. The following antibodies were used: anti-GFP (chicken; Aves, Tigard, OR) and peroxidase-conjugated donkey anti-chicken antibodies (Jackson ImmunoResearch Laboratories, West Grove, PA).

Construction of expression vectors, transfections, and lentiviral infections

Eukaryotic expression plasmids for tau deletion constructs, tau isoforms, and tau mutants (S396A/S404A, S396E/S404E, G389R, K369I) with amino-terminally fused PAGFP tag were constructed in pRc/cytomegalovirus (CMV)-based expression vectors (Life Technologies, Carlsbad, CA) containing a CMV promoter and kanamycin and neomycin resistance genes. Constructs coding for tau441PHP and the respective wt control were constructed in pSems-based expression vectors (Wilmes *et al.*, 2012). Deletion constructs were constructed by addition of stop codons (TAA for tau Δ 276, Δ 307, Δ 338, Δ 369, and tau352 Δ 280 and TAG for tau Δ 401) at the indicated position. The pCMV-3 \times PAGFP plasmid was described previously (Weissmann *et al.*, 2009). Lentiviral vectors for tau441wt with amino-terminally fused PAGFP tag were constructed in L22FCK(1.3)GW (provided by P. Osten, Northwestern University, Chicago, IL), which contains the neuron-specific promoter α -CaMKII (Dittgen *et al.*, 2004). Sequences that were introduced by PCR were verified by DNA sequencing (Seqlab-Microsynth, Göttingen, Germany).

Transfections of PC12 cells were performed with Lipofectamine 2000 (Invitrogen) essentially as described previously (Fath *et al.*, 2002). For production of lentivirus, human embryonic kidney cells 293FT (Life Technologies) were transfected with the expression vector and two helper plasmids, and viral particles from the supernatant were concentrated by ultracentrifugation as described previously (Bakota *et al.*, 2012).

Cell culture and live-cell labeling

PC12 cells were cultured in serum-DMEM as described previously (Fath *et al.*, 2002). Undifferentiated cells were plated on 35-mm poly-L-lysine- and collagen-coated glass-bottom culture dishes (MatTek, Ashland, MA) at 10^3 – 10^4 cells/cm² and cultured in DMEM with 1% (vol/vol) serum without phenol red. For total internal reflection fluorescence (TIRF) imaging, cells were plated on glass coverslips (24 mm, No. 1; VWR, Radnor, PA) coated with a poly-L-lysine-graft-(polyethylene glycol) copolymer functionalized with RGD as described previously (VandeVondele *et al.*, 2003). For neuronal differentiation, cells were treated with 100 ng/ml 7S mouse nerve growth factor (Alomone Laboratories, Munich, Germany) for 4–6 d, and the medium was changed after 2–3 d. Primary cortical cultures were prepared from cerebral cortices of mouse embryos (days 14–16 of gestation) and cultured as described previously (Bakota *et al.*, 2012). The cultures were obtained from *TAU*^{-/-} mice (Dawson *et al.*, 2001) on a C57BL/6 background. Cells were plated at 2.5×10^4 cells/cm² on polylysine- and laminin-coated coverslips. For imaging, the medium was exchanged against NEUMO with supplements for neuronal cells as described in the user guidelines of the manufacturer (Cell Guidance Systems, Cambridge, United Kingdom).

Labeling of PC12 cells for TIRF imaging was performed by incubation with serum-DMEM containing 1–5 nM tetramethylrhodamine-HaloTag ligand for 15 min at 37°C. This corresponded to a labeling efficiency of <0.02% of the exogenous Halo-tau. Subsequently, cells were washed with serum-DMEM without phenol red and then left to recover for 30 min in the incubator, followed by an additional medium exchange. All animals were maintained and killed according to National Institutes of Health guidelines and German animal care regulations.

Photoactivation and live imaging

Live imaging was performed using a laser scanning microscope (Eclipse TE2000-U inverted; Nikon, Tokyo, Japan) equipped with argon (488-nm) and blue diode (405-nm) lasers. PAGFP-tau-expressing cells were visualized with a Fluor 60x (numerical aperture [NA] 1.4) ultraviolet-corrected objective lens. The microscope was enclosed in an incubation chamber maintained at 37°C and 5% CO₂ (Solent Scientific, Fareham, United Kingdom). Automated image acquisition after photoactivation was essentially performed as described previously (Igaev *et al.*, 2014). Photoactivation of a neurite's segment of ~6 μm in length was performed with a blue diode. A set of consecutive images (time stack) was obtained at a frequency of 1 frame/s, and 112 frames were collected per experiment. All stacks were collected at a resolution of 256 × 256 pixels.

Single-molecule microscopy, localization, and tracking

For performing single-molecule experiments, TIRF microscopy was performed using an Olympus excellence cell TIRF microscope equipped with 561-nm (200-mW) laser (Olympus, Tokyo, Japan) and a back-illuminated electron-multiplied charge-coupled device camera (C9100-13; Hamamatsu, Hamamatsu City, Japan). Fast single-molecule tracking used a digital complementary metal-oxide-semiconductor camera (ORCA-Flash4.0 V2 C11440-22CU; Hamamatsu). A 150x magnification objective with NA 1.45 (UAPON 150x/1.45; Olympus) was used for TIR illumination. The emitted light from the sample was filtered using a quad-band bandpass filter (FF01 446/523/600/677; Semrock, Rochester, NY). The microscope was enclosed in an incubation chamber maintained at 37°C and 5% CO₂ (Olympus-PeCon). Localization and trajectory reconstruction were carried out as previously described (Janning *et al.*, 2014). The theo-

retical localization precision of Halo-tau was 16.7 ± 0.2 nm. For further analysis, a mask was placed over the cell processes, and trajectories outside of this mask were removed.

Dwell-time determination

The dwell time of tau in the MT-bound state was determined by counting how many consecutive frames a single localized signal stayed within a radius of 50 nm. The respective frequency histograms were fitted by a single exponential to obtain the dwell time.

FDAP data analysis

Effective diffusion constants were determined by fitting the data from photoactivation experiments by a model FDAP function described in Weissmann *et al.* (2009). To estimate directly the pseudo-first-order association rate ($k_{on}^* = k_{on}[MT]_{eq}$, where $[MT]_{eq}$ is the equilibrium concentration of tau binding sites on MTs) and the dissociation rate (k_{off}) of tau to/from MTs, we used a reaction-diffusion model of the tau-MT kinetics as described in Igaev *et al.* (2014). Analysis of individual FDAP curves was performed with a custom C-based tool called *cFDAP* (www.github.com/moozzz/cFDAP). The tool uses the Levenberg-Marquardt algorithm to solve the weighted and unweighted problems of multidimensional nonlinear least-square fitting (Moré, 1978) implemented in the GNU Scientific Library (Galassi *et al.*, 2009). Generally, the problem reads as follows:

$$\chi^2(\boldsymbol{\beta}) = \frac{1}{2} \sum_i \omega_i [f(t_i) - \text{FDAP}(t_i, \boldsymbol{\beta})]^2 \quad (1)$$

where $f(t)$ represents the average of several FDAP curves sampled on a time set t_i , $\text{FDAP}(t, \boldsymbol{\beta})$ is a model FDAP function also sampled on t_i , $\boldsymbol{\beta}$ is a vector of parameters to be varied during the fitting procedure (in our case, $\boldsymbol{\beta} = (k_{on}^*, k_{off})$), $\omega_i = 1/\sigma_i^2$, and σ_i is the error for the i th time point. Because all FDAP curves were analyzed individually, the unweighted scheme was chosen, in which $\omega_i \equiv 1$. The Levenberg-Marquardt algorithm iteratively minimizes the function in (1). To start the minimization, the user has to provide an initial guess for the parameter vector. In each iteration step, the parameter vector $\boldsymbol{\beta}$ is then replaced by $\boldsymbol{\beta} + \Delta\boldsymbol{\beta}$, and the FDAP model function is approximated by a linearization:

$$\text{FDAP}(t_i, \boldsymbol{\beta}) \approx \text{FDAP}(t_i, \boldsymbol{\beta}) + J_i \Delta\boldsymbol{\beta} \quad (2)$$

where $J_i = \partial \text{FDAP}(t_i, \boldsymbol{\beta}) / \partial \boldsymbol{\beta}$ is the gradient of $\text{FDAP}(t, \boldsymbol{\beta})$ with respect to $\boldsymbol{\beta}$. At the minimum of the sum of squared residuals (1), the gradient (2) is expected to be zero. The theoretical basis underlying the model FDAP functions used in the present work was given previously (Igaev *et al.*, 2014). The fitting procedure was used to extract k_{on}^* and k_{off} from every single FDAP curve for every tau construct. The χ^2 value was used as an indicator of goodness of fit. All of the three values (k_{on}^* , k_{off} , and χ^2) are independent and, in fact, random values with certain distributions. Hence, before computing averages or comparing the binding parameters for different tau constructs with each other, we needed to ensure that the obtained k_{on}^* , k_{off} , and χ^2 samples contained no statistical outliers (SOs). We used the following protocol to exclude SOs. First, we verified whether all of the three parameters were normally distributed. The D'Agostino-Pearson test for normality showed that the majority of the samples are not normally distributed ($p < 0.9$). However, upon a logarithmic transformation ($\ln(k_{on}^*)$, $\ln(k_{off})$, and $\ln(\chi^2)$), all of the tested samples demonstrated high p values ($p > 0.9$) in the D'Agostino-Pearson test. We thus concluded that k_{on}^* , k_{off} , and χ^2 are log-normally distributed values. For all subsequent analyses, the samples were logarithmically transformed, and only the transformed samples were

further processed. We then verified whether there was a linear statistical correlation between $\ln(k_{\text{on}}^*)$ and $\ln(\chi^2)$ and between $\ln(k_{\text{off}})$ and $\ln(\chi^2)$. For the majority of tau constructs, the mentioned sample pairs were highly uncorrelated ($R^2 < 0.1$), and only a minority showed a weak correlation ($R^2 \sim 0.1\text{--}0.2$). This allowed us to conclude that both $\ln(k_{\text{on}}^*)$ and $\ln(k_{\text{off}})$ samples are linearly statistically independent of $\ln(\chi^2)$ and perform the subsequent SO detection independently for $\ln(k_{\text{on}}^*)$, $\ln(k_{\text{off}})$, and $\ln(\chi^2)$. Finally, we eliminated SOs in the $\ln(\chi^2)$ samples by using Iglewicz and Hoaglin's robust test, as those SOs represented bad fits and had to be removed first. Then we repeated this procedure for $\ln(k_{\text{on}}^*)$ and $\ln(k_{\text{off}})$.

Bioinformatic analysis

Definition of the PRR. We followed the definition by Chapin and Bulinski (1992), who reported the presence of an extra 14-amino acid spacer segment directly after the fourth repeat region (RR4) of tau followed by a truncated repeat. The PRR was defined as a motif starting directly after RR4 and extending to the same length as an RR (31 amino acids).

Analysis of the relationship between the RRs and the PRR. The relation between the different RRs and the PRR was determined by a cluster analysis of the amino acid sequences of the respective regions. The sequences of the RRs and the PRR were automatically identified by HMM-based search (Eddy, 1998; Finn et al., 2011) of the generalized Pfam (Finn et al., 2016) from tau and MAP tubulin-binding repeats (PF00418, tubulin-binding, tau, and MAP protein, tubulin-binding repeat) versus a previously manually cured collection of 49 mammalian full-length sequences (776 amino acids in length). The generalized Pfam HMM was created with the *hmmbuild* tool of the HMMER 3.1b2 package and was based on a seed alignment (114 sequences) of the PF00418 entry. The resulting hits were extracted by a self-written python script with the help of the *biopython* library (Python Software Foundation, www.python.org/psf/; Cock et al., 2009). The resulting hits were collected in a single file, and a cluster analysis was performed in the R software suite with the help of the *phangorn* package (R Development Core Team, 2008; Schliep, 2011). The distance matrix for the cluster analysis was calculated using the Johns–Tyler–Thornton model of amino acid evolution (Jones et al., 1992). The clusters were generated by a neighbor-joining algorithm (Saitou and Nei, 1987) implemented in the *phangorn* package. Supporting bootstrap values for the splits were generated by 10^4 replications, and the majority-rule consensus tree was created by the *sumtree.py* software (Sukumaran and Holder, 2010). The tree was converted into an unrooted tree to visualize the grouping using the *dendroscope* software (Huson and Scornavacca, 2012).

Definition of the SM and HMM-HMM comparisons. To determine the part of the PRR that shows the largest similarity to the RRs, we used a HMM-HMM comparison method as proposed by Soding (2005). The Pfam generalized HMM was used as a query HMM. To determine the size of the SM, an iterative comparison approach was chosen. The number of columns of the target alignment (sequence following the fourth repeat) was iteratively increased one amino acid per step, and the corresponding HMM was built and compared with the query Pfam HMM. The maximum probability was reached when the SM was 18 amino acids long. This value (18 amino acids) was used to set the border of the SM. The alignment was then used to build a HMM, which was visualized as a HMM logo by the *skyalign* package (Eddy, 1998; Wheeler et al., 2014). The previously derived PRR-HMM was compared with the HMM of other classes (Aves, 15 sequences; Reptilia, 12 sequences; Actinopterygii, 16 sequences), as well as with

general HMMs of MAP2 (87 sequences from all classes) and MAP4 (110 sequences from all classes; Soding, 2005; Sundermann et al., 2016). All of the mentioned HMMs (MAPT/2/4) were based on manually cured sequence reconstructions.

Visualization of the three-dimensional structure of tau. A representative three-dimensional (3D) structure of tau (441-aa isoform) was generated by Random Coil Generator (RCG) software (Jha et al., 2005). The random coil model is frequently used to generate conformational ensembles of intrinsically disordered proteins. In the RCG model, intramolecular interactions are neglected, and only backbone conformational frequencies from the coil library of the Protein Data Bank (www.rcsb.org/) are used to generate the ensemble. The domain organization was mapped onto the 3D structure. Visualization and structure rendering was performed using the Visual Molecular Dynamics package as surface representation (Humphrey et al., 1996).

Other methods

SDS–PAGE and immunoblot analysis by enhanced chemiluminescence were performed as described previously (Leschik et al., 2007). Cellular lysates were prepared in radioimmunoprecipitation assay buffer (50 mM Tris/HCl, pH 7.5, 150 mM NaCl, 1 mM EDTA, 1% NP-40, 0.5% deoxycholate, and 0.1% SDS) containing protease inhibitors (1 mM phenylmethylsulfonyl fluoride, 10 $\mu\text{g}/\text{ml}$ each leupeptin and pepstatin, and 1 mM ethylene glycol tetraacetic acid), and 20 μg of total protein were loaded per lane. Protein concentration was determined using a bicinchoninic acid protein assay kit (Thermo Fisher Scientific, Waltham, MA). Statistical analysis was performed using two-tailed, unpaired Student's *t* test. The α -levels were defined as follows: * $p < 0.05$, ** $p < 0.01$, and *** $p < 0.001$.

ACKNOWLEDGMENTS

We thank Anne Gauthier-Kemper for preparing the lentiviral vector and Rainer Kurre for assistance with microscopy devices. This work was supported by the Z-project of the SFB 944, University of Osnabrück, computing time by the Norddeutscher Verbund für Hoch- und Höchstleistungsrechnen, and the UV2000/GPU cluster at the computing center of the University of Osnabrück.

REFERENCES

- Augustinack JC, Schneider A, Mandelkow EM, Hyman BT (2002). Specific tau phosphorylation sites correlate with severity of neuronal cytopathology in Alzheimer's disease. *Acta Neuropathol* 103, 26–35.
- Baas PW, Deitch JS, Black MM, Banker GA (1988). Polarity orientation of microtubules in hippocampal neurons: uniformity in the axon and non-uniformity in the dendrite. *Proc Natl Acad Sci USA* 85, 8335–8339.
- Bakota L, Brandt R (2016). Tau biology and tau-directed therapies for Alzheimer's disease. *Drugs* 76, 301–313.
- Bakota L, Brandt R, Heinisch JJ (2012). Triple mammalian/yeast/bacterial shuttle vectors for single and combined Lentivirus- and Sindbis virus-mediated infections of neurons. *Mol Genet Genomics* 287, 313–324.
- Bermingham N, Cowie TF, Paine M, Storey E, McLean C (2008). Frontotemporal dementia and Parkinsonism linked to chromosome 17 in a young Australian patient with the G389R Tau mutation. *Neuropathol Appl Neurobiol* 34, 366–370.
- Bodea LG, Eckert A, Ittner LM, Piguot O, Gotz J (2016). Tau physiology and pathomechanisms in frontotemporal lobar degeneration. *J Neurochem* 138, (Suppl 1)71–94.
- Boutajangout A, Ingadottir J, Davies P, Sigurdsson EM (2011). Passive immunization targeting pathological phospho-tau protein in a mouse model reduces functional decline and clears tau aggregates from the brain. *J Neurochem* 118, 658–667.
- Brandt R, Gergou A, Wacker I, Fath T, Hutter H (2009). A Caenorhabditis elegans model of tau hyperphosphorylation: induction of developmental

- defects by transgenic overexpression of Alzheimer's disease-like modified tau. *Neurobiol Aging* 30, 22–33.
- Brandt R, Lee G (1993). Functional organization of microtubule-associated protein tau. Identification of regions which affect microtubule growth, nucleation, and bundle formation in vitro. *J Biol Chem* 268, 3414–3419.
- Bunker JM, Wilson L, Jordan MA, Feinstein SC (2004). Modulation of microtubule dynamics by tau in living cells: implications for development and neurodegeneration. *Mol Biol Cell* 15, 2720–2728.
- Butner KA, Kirschner MW (1991). Tau protein binds to microtubules through a flexible array of distributed weak sites. *J Cell Biol* 115, 717–730.
- Cash AD, Aliev G, Siedlak SL, Nunomura A, Fujioka H, Zhu X, Raina AK, Vinters HV, Tabaton M, Johnson AB, et al. (2003). Microtubule reduction in Alzheimer's disease and aging is independent of tau filament formation. *Am J Pathol* 162, 1623–1627.
- Chapin SJ, Bulinski JC (1992). Microtubule stabilization by assembly-promoting microtubule-associated proteins: a repeat performance. *Cell Motil Cytoskeleton* 23, 236–243.
- Chaunu MP, Deramecourt V, Buee-Scherrer V, Le Ber I, Brice A, Ehrle N, El Hachimi K, Pluot M, Maurage CA, Bakchine S, et al. (2013). Juvenile frontotemporal dementia with parkinsonism associated with tau mutation G389R. *J Alzheimers Dis* 37, 769–776.
- Chen J, Kanai Y, Cowan NJ, Hirokawa N (1992). Projection domains of MAP2 and tau determine spacings between microtubules in dendrites and axons. *Nature* 360, 674–677.
- Chung PJ, Choi MC, Miller HP, Feinstein HE, Raviv U, Li Y, Wilson L, Feinstein SC, Safinya CR (2015). Direct force measurements reveal that protein Tau confers short-range attractions and isoform-dependent steric stabilization to microtubules. *Proc Natl Acad Sci USA* 112, E6416–E6425.
- Cock PJ, Antao T, Chang JT, Chapman BA, Cox CJ, Dalke A, Friedberg I, Hamelryck T, Kauff F, Wilczynski B, de Hoon MJ (2009). Biopython: freely available Python tools for computational molecular biology and bioinformatics. *Bioinformatics* 25, 1422–1423.
- Combs B, Voss K, Gamblin TC (2011). Pseudohyperphosphorylation has differential effects on polymerization and function of tau isoforms. *Biochemistry* 50, 9446–9456.
- Dawson HN, Ferreira A, Eyster MV, Ghoshal N, Binder LI, Vitek MP (2001). Inhibition of neuronal maturation in primary hippocampal neurons from tau deficient mice. *J Cell Sci* 114, 1179–1187.
- Dehmelt L, Halpain S (2005). The MAP2/Tau family of microtubule-associated proteins. *Genome Biol* 6, 204.
- Derisbourg M, Leghay C, Chiappetta G, Fernandez-Gomez FJ, Laurent C, Demeyer D, Carrier S, Buee-Scherrer V, Blum D, Vinh J, et al. (2015). Role of the Tau N-terminal region in microtubule stabilization revealed by new endogenous truncated forms. *Sci Rep* 5, 9659.
- Ding H, Matthews TA, Johnson GV (2006). Site-specific phosphorylation and caspase cleavage differentially impact tau-microtubule interactions and tau aggregation. *J Biol Chem* 281, 19107–19114.
- Dittgen T, Nimmerjahn A, Komai S, Licznernski P, Waters J, Margrie TW, Helmchen F, Denk W, Brecht M, Osten P (2004). Lentivirus-based genetic manipulations of cortical neurons and their optical and electrophysiological monitoring in vivo. *Proc Natl Acad Sci USA* 101, 18206–18211.
- Duan AR, Goodson HV (2012). Taxol-stabilized microtubules promote the formation of filaments from unmodified full-length Tau in vitro. *Mol Biol Cell* 23, 4796–4806.
- Eddy SR (1998). Profile hidden Markov models. *Bioinformatics* 14, 755–763.
- Eidenmuller J, Fath T, Hellwig A, Reed J, Sontag E, Brandt R (2000). Structural and functional implications of tau hyperphosphorylation: information from phosphorylation-mimicking mutated tau proteins. *Biochemistry* 39, 13166–13175.
- Eidenmuller J, Fath T, Maas T, Pool M, Sontag E, Brandt R (2001). Phosphorylation-mimicking glutamate clusters in the proline-rich region are sufficient to simulate the functional deficiencies of hyperphosphorylated tau protein. *Biochem J* 357, 759–767.
- Fath T, Eidenmuller J, Brandt R (2002). Tau-mediated cytotoxicity in a pseudohyperphosphorylation model of Alzheimer's disease. *J Neurosci* 22, 9733–9741.
- Finn RD, Clements J, Eddy SR (2011). HMMER web server: interactive sequence similarity searching. *Nucleic Acids Res* 39, W29–37.
- Finn RD, Coghill P, Eberhardt RY, Eddy SR, Mitchell AL, Potter SC, Punta M, Qureshi M, Sangrador-Vegas A, et al. (2016). The Pfam protein families database: towards a more sustainable future. *Nucleic Acids Res* 44, D279–D285.
- Flores-Rodriguez P, Ontiveros-Torres MA, Cardenas-Aguayo MC, Luna-Arias JP, Meraz-Rios MA, Viramontes-Pintos A, Harrington CR, Wischik CM, Mena R, Floran-Garduno B, Luna-Munoz J (2015). The relationship between truncation and phosphorylation at the C-terminus of tau protein in the paired helical filaments of Alzheimer's disease. *Front Neurosci* 9, 33.
- Galassi M, Davies J, Theiler J, Gough B, Jungman G, Alken P, Booth M, Rossi F (2009). GNU Scientific Library Reference Manual, Godalming, United Kingdom: Network Theory Ltd.
- Gamblin TC, Chen F, Zambrano A, Abraha A, Lagalwar S, Guillozet AL, Lu M, Fu Y, Garcia-Sierra F, LaPointe N, et al. (2003). Caspase cleavage of tau: linking amyloid and neurofibrillary tangles in Alzheimer's disease. *Proc Natl Acad Sci USA* 100, 10032–10037.
- Gauthier-Kemper A, Weissmann C, Golovyashkina N, Sebo-Lemke Z, Drewes G, Gerke V, Heinisch JJ, Brandt R (2011). The frontotemporal dementia mutation R406W blocks tau's interaction with the membrane in an annexin A2-dependent manner. *J Cell Biol* 192, 647–661.
- Ghetti B, Murrell JR, Zolo P, Spillantini MG, Goedert M (2000). Progress in hereditary tauopathies: a mutation in the Tau gene (G389R) causes a Pick disease-like syndrome. *Ann NY Acad Sci* 920, 52–62.
- Golovyashkina N, Penazzi L, Ballatore C, Smith AB 3rd, Bakota L, Brandt R (2015). Region-specific dendritic simplification induced by Abeta, mediated by tau via dysregulation of microtubule dynamics: a mechanistic distinct event from other neurodegenerative processes. *Mol Neurodegener* 10, 60.
- Goode BL, Chau M, Denis PE, Feinstein SC (2000). Structural and functional differences between 3-repeat and 4-repeat tau isoforms. Implications for normal tau function and the onset of neurodegenerative disease. *J Biol Chem* 275, 38182–38189.
- Goode BL, Feinstein SC (1994). Identification of a novel microtubule binding and assembly domain in the developmentally regulated inter-repeat region of tau. *J Cell Biol* 124, 769–782.
- Gustke N, Trinczek B, Biernat J, Mandelkow EM, Mandelkow E (1994). Domains of tau protein and interactions with microtubules. *Biochemistry* 33, 9511–9522.
- Hasegawa M, Morishima-Kawashima M, Takio K, Suzuki M, Titani K, Ihara Y (1992). Protein sequence and mass spectrometric analyses of tau in the Alzheimer's disease brain. *J Biol Chem* 267, 17047–17054.
- Heidemann SR, Landers JM, Hamborg MA (1981). Polarity orientation of axonal microtubules. *J Cell Biol* 91, 661–665.
- Hirokawa N (1982). Cross-linker system between neurofilaments, microtubules, and membranous organelles in frog axons revealed by the quick-freeze, deep-etching method. *J Cell Biol* 94, 129–142.
- Humphrey W, Dalke A, Schulten K (1996). VMD: visual molecular dynamics. *J Mol Graph* 14, 33–38.
- Hundelt M, Fath T, Selle K, Oesterwind K, Jordan J, Schultz C, Gotz J, von Engelhardt J, Monyer H, Lewejohann L, et al. (2011). Altered phosphorylation but no neurodegeneration in a mouse model of tau hyperphosphorylation. *Neurobiol Aging* 32, 991–1006.
- Huson DH, Scornavacca C (2012). Dendroscope 3: an interactive tool for rooted phylogenetic trees and networks. *Syst Biol* 61, 1061–1067.
- Igaev M, Janning D, Sundermann F, Niewidok B, Brandt R, Junge W (2014). A refined reaction-diffusion model of tau-microtubule dynamics and its application in FDAP analysis. *Biophys J* 107, 2567–2578.
- Janning D, Igaev M, Sundermann F, Bruhmann J, Beutel O, Heinisch JJ, Bakota L, Piehler J, Junge W, Brandt R (2014). Single-molecule tracking of tau reveals fast kiss-and-hop interaction with microtubules in living neurons. *Mol Biol Cell* 25, 3541–3551.
- Jeganathan S, Hascher A, Chinnathambi S, Biernat J, Mandelkow EM, Mandelkow E (2008). Proline-directed pseudo-phosphorylation at AT8 and PHF1 epitopes induces a compaction of the paperclip folding of Tau and generates a pathological (MC-1) conformation. *J Biol Chem* 283, 32066–32076.
- Jha AK, Colubri A, Freed KF, Sosnick TR (2005). Statistical coil model of the unfolded state: resolving the reconciliation problem. *Proc Natl Acad Sci USA* 102, 13099–13104.
- Jones DT, Taylor WR, Thornton JM (1992). The rapid generation of mutation data matrices from protein sequences. *Comput Appl Biosci* 8, 275–282.
- Kadavath H, Hofele RV, Biernat J, Kumar S, Tepper K, Urlaub H, Mandelkow E, Zweckstetter M (2015a). Tau stabilizes microtubules by binding at the interface between tubulin heterodimers. *Proc Natl Acad Sci USA* 112, 7501–7506.
- Kadavath H, Jaremko M, Jaremko L, Biernat J, Mandelkow E, Zweckstetter M (2015b). Folding of the tau protein on microtubules. *Angew Chem Int Ed Engl* 54, 10347–10351.
- Kanmert D, Cantlon A, Muratore CR, Jin M, O'Malley TT, Lee G, Young-Pearse TL, Selkoe DJ, Walsh DM (2015). C-terminally truncated forms of tau, but not full-length tau or its c-terminal fragments, are released from neurons independently of cell death. *J Neurosci* 35, 10851–10865.

- Kiris E, Ventimiglia D, Sargin ME, Gaylord MR, Altinok A, Rose K, Manjunath BS, Jordan MA, Wilson L, Feinstein SC (2011). Combinatorial tau pseudophosphorylation: markedly different regulatory effects on microtubule assembly and dynamic instability than the sum of the individual parts. *J Biol Chem* 286, 14257–14270.
- Konzack S, Thies E, Marx A, Mandelkow EM, Mandelkow E (2007). Swimming against the tide: mobility of the microtubule-associated protein tau in neurons. *J Neurosci* 27, 9916–9927.
- Lang AE, Riherd Methner DN, Ferreira A (2014). Neuronal degeneration, synaptic defects, and behavioral abnormalities in tau(4)(5)(-)(2)(3)(0) transgenic mice. *Neuroscience* 275, 322–339.
- Lee G, Neve RL, Kosik KS (1989). The microtubule binding domain of tau protein. *Neuron* 2, 1615–1624.
- Leger JG, Brandt R, Lee G (1994). Identification of tau protein regions required for process formation in PC12 cells. *J Cell Sci* 107, 3403–3412.
- Leschik J, Welzel A, Weissmann C, Eckert A, Brandt R (2007). Inverse and distinct modulation of tau-dependent neurodegeneration by presenilin 1 and amyloid-beta in cultured cortical neurons: evidence that tau phosphorylation is the limiting factor in amyloid-beta-induced cell death. *J Neurochem* 101, 1303–1315.
- Lewis J, Dickson DW (2016). Propagation of tau pathology: hypotheses, discoveries, and yet unresolved questions from experimental and human brain studies. *Acta Neuropathol* 131, 27–48.
- Lewis J, McGowan E, Rockwood J, Melrose H, Nacharaju P, Van Slegtenhorst M, Gwinn-Hardy K, Paul Murphy M, Baker M, Yu X, et al. (2000). Neurofibrillary tangles, amyotrophy and progressive motor disturbance in mice expressing mutant (P301L) tau protein. *Nat Genet* 25, 402–405.
- Maas T, Eidenmuller J, Brandt R (2000). Interaction of tau with the neural membrane cortex is regulated by phosphorylation at sites that are modified in paired helical filaments. *J Biol Chem* 275, 15733–15740.
- Mandell JW, Banker GA (1996). A spatial gradient of tau protein phosphorylation in nascent axons. *J Neurosci* 16, 5727–5740.
- Mondragon-Rodriguez S, Perry G, Luna-Munoz J, Acevedo-Aquino MC, Williams S (2014). Phosphorylation of tau protein at sites Ser(396–404) is one of the earliest events in Alzheimer's disease and Down syndrome. *Neuropathol Appl Neurobiol* 40, 121–135.
- Moré JJ (1978). The Levenberg-Marquardt algorithm: implementation and theory. In: *Numerical Analysis*, ed. GA Watson, Berlin: Springer-Verlag, 105–116.
- Morishima-Kawashima M, Hasegawa M, Takio K, Suzuki M, Yoshida H, Titani K, Ihara Y (1995). Proline-directed and non-proline-directed phosphorylation of PHF-tau. *J Biol Chem* 270, 823–829.
- Morris M, Knudsen GM, Maeda S, Trinidad JC, Ioanoviciu A, Burlingame AL, Mucke L (2015). Tau post-translational modifications in wild-type and human amyloid precursor protein transgenic mice. *Nat Neurosci* 18, 1183–1189.
- Neumann M, Schulz-Schaeffer W, Crowther RA, Smith MJ, Spillantini MG, Goedert M, Kretschmar HA (2001). Pick's disease associated with the novel Tau gene mutation K369I. *Ann Neurol* 50, 503–513.
- Nogales E, Wolf SG, Khan IA, Luduena RF, Downing KH (1995). Structure of tubulin at 6.5 Å and location of the taxol-binding site. *Nature* 375, 424–427.
- Okabe S, Hirokawa N (1988). Microtubule dynamics in nerve cells: analysis using microinjection of biotinylated tubulin into PC12 cells. *J Cell Biol* 107, 651–664.
- Otvos L Jr, Feiner L, Lang E, Szendrei GI, Goedert M, Lee VM (1994). Monoclonal antibody PHF-1 recognizes tau protein phosphorylated at serine residues 396 and 404. *J Neurosci Res* 39, 669–673.
- Panda D, Samuel JC, Massie M, Feinstein SC, Wilson R (2003). Differential regulation of microtubule dynamics by three- and four-repeat tau: implications for the onset of neurodegenerative disease. *Proc Natl Acad Sci USA* 100, 9548–9553.
- Papasozomenos SC, Binder LI (1987). Phosphorylation determines two distinct species of Tau in the central nervous system. *Cell Motil Cytoskeleton* 8, 210–226.
- Park SY, Ferreira A (2005). The generation of a 17 kDa neurotoxic fragment: an alternative mechanism by which tau mediates beta-amyloid-induced neurodegeneration. *J Neurosci* 25, 5365–5375.
- Patterson GH, Lippincott-Schwartz J (2002). A photoactivatable GFP for selective photolabeling of proteins and cells. *Science* 297, 1873–1877.
- Penazzi L, Bakota L, Brandt R (2016a). Microtubule dynamics in neuronal development, plasticity, and neurodegeneration. *Int Rev Cell Mol Biol* 321, 89–169.
- Penazzi L, Tackenberg C, Ghori A, Golovyashkina N, Niewidok B, Selle K, Ballatore C, Smith AB 3rd, Bakota L, Brandt R (2016b). Abeta-mediated spine changes in the hippocampus are microtubule-dependent and can be reversed by a subnanomolar concentration of the microtubule-stabilizing agent epothilone D. *Neuropharmacology* 105, 84–95.
- Preuss U, Biernat J, Mandelkow EM, Mandelkow E (1997). The “jaws” model of tau-microtubule interaction examined in CHO cells. *J Cell Sci* 110, 789–800.
- Rapoport M, Dawson HN, Binder LI, Vitek MP, Ferreira A (2002). Tau is essential to beta-amyloid-induced neurotoxicity. *Proc Natl Acad Sci USA* 99, 6364–6369.
- Rapoport M, Ferreira A (2000). PD98059 prevents neurite degeneration induced by fibrillar beta-amyloid in mature hippocampal neurons. *J Neurochem* 74, 125–133.
- R Development Core Team (2008). R: a language and environment for statistical computing, Vienna, Austria: R Foundation for Statistical Computing. www.R-project.org.
- Reifert J, Hartung-Cranston D, Feinstein SC (2011). Amyloid beta-mediated cell death of cultured hippocampal neurons reveals extensive tau fragmentation without increased full-length tau phosphorylation. *J Biol Chem* 286, 20797–20811.
- Roberson ED, Scearce-Levie K, Palop JJ, Yan F, Cheng IH, Wu T, Gerstein H, Yu GQ, Mucke L (2007). Reducing endogenous tau ameliorates amyloid beta-induced deficits in an Alzheimer's disease mouse model. *Science* 316, 750–754.
- Saitou N, Nei M (1987). The neighbor-joining method: a new method for reconstructing phylogenetic trees. *Mol Biol Evol* 4, 406–425.
- Samsonov A, Yu JZ, Rasenick M, Popov SV (2004). Tau interaction with microtubules in vivo. *J Cell Sci* 117, 6129–6141.
- Schliep KP (2011). phangorn: phylogenetic analysis in R. *Bioinformatics* 27, 592–593.
- Shahani N, Subramaniam S, Wolf T, Tackenberg C, Brandt R (2006). Tau aggregation and progressive neuronal degeneration in the absence of changes in spine density and morphology after targeted expression of Alzheimer's disease-relevant tau constructs in organotypic hippocampal slices. *J Neurosci* 26, 6103–6114.
- Soding J (2005). Protein homology detection by HMM-HMM comparison. *Bioinformatics* 21, 951–960.
- Spillantini MG, Goedert M (2013). Tau pathology and neurodegeneration. *Lancet Neurol* 12, 609–622.
- Sprague BL, Pego RL, Stavreva DA, McNally JG (2004). Analysis of binding reactions by fluorescence recovery after photobleaching. *Biophys J* 86, 3473–3495.
- Stoothoff W, Jones PB, Spiers-Jones TL, Joyner D, Chhabra E, Bercury K, Fan Z, Xie H, Bacskai B, Edd J, Hyman BT (2009). Differential effect of three-repeat and four-repeat tau on mitochondrial axonal transport. *J Neurochem* 111, 417–427.
- Sukumaran J, Holder MT (2010). DendroPy: a Python library for phylogenetic computing. *Bioinformatics* 26, 1569–1571.
- Sundermann F, Fernandez MP, Morgan RO (2016). An evolutionary roadmap to the microtubule-associated protein MAP Tau. *BMC Genomics* 17, 264.
- Tackenberg C, Brandt R (2009). Divergent pathways mediate spine alterations and cell death induced by amyloid-beta, wild-type tau, and R406W tau. *J Neurosci* 29, 14439–14450.
- VandeVondele S, Voros J, Hubbell JA (2003). RGD-grafted poly-L-lysine-graft-(polyethylene glycol) copolymers block non-specific protein adsorption while promoting cell adhesion. *Biotechnol Bioeng* 82, 784–790.
- Watanabe A, Hasegawa M, Suzuki M, Takio K, Morishima-Kawashima M, Titani K, Arai T, Kosik KS, Ihara Y (1993). In vivo phosphorylation sites in fetal and adult rat tau. *J Biol Chem* 268, 25712–25717.
- Weissmann C, Reyher HJ, Gauthier A, Steinhoff HJ, Junge W, Brandt R (2009). Microtubule binding and trapping at the tip of neurites regulate tau motion in living neurons. *Traffic* 10, 1655–1668.
- Wheeler TJ, Clements J, Finn RD (2014). Skyclign: a tool for creating informative, interactive logos representing sequence alignments and profile hidden Markov models. *BMC Bioinformatics* 15, 7.
- Wilmes S, Staufenbiel M, Lisse D, Richter CP, Beutel O, Busch KB, Hess ST, Piehler J (2012). Triple-color super-resolution imaging of live cells: resolving submicroscopic receptor organization in the plasma membrane. *Angew Chem Int Ed Engl* 51, 4868–4871.
- Wischik CM, Novak M, Thogersen HC, Edwards PC, Runswick MJ, Jakes R, Walker JE, Milstein C, Roth M, Klug A (1988). Isolation of a fragment of tau derived from the core of the paired helical filament of Alzheimer disease. *Proc Natl Acad Sci USA* 85, 4506–4510.
- Xia D, Li C, Gotz J (2015). Pseudophosphorylation of Tau at distinct epitopes or the presence of the P301L mutation targets the microtubule-associated protein Tau to dendritic spines. *Biochim Biophys Acta* 1852, 913–924.
- Xiao H, Verdier-Pinard P, Fernandez-Fuentes N, Burd B, Angeletti R, Fiser A, Horwitz SB, Orr GA (2006). Insights into the mechanism of microtubule stabilization by Taxol. *Proc Natl Acad Sci USA* 103, 10166–10173.